

RESEARCH ARTICLE | JUNE 16 2021

Characterizing materials for superconducting radiofrequency applications—A comprehensive overview of the quadrupole resonator design and measurement capabilities

S. Keckert   ; R. Kleindienst; O. Kugeler  ; D. Tikhonov  ; J. Knobloch 

 Check for updates

Rev. Sci. Instrum. 92, 064710 (2021)

<https://doi.org/10.1063/5.0046971>



View
Online



Export
Citation

CrossMark

Articles You May Be Interested In

Mitigation of parasitic losses in the quadrupole resonator enabling direct measurements of low residual resistances of SRF samples

AIP Advances (December 2021)

Radiation pressure efficiency measurements of nanoparticle coated microspheres

Appl. Phys. Lett. (December 2013)

Comparison of model and neural responses to speech

J Acoust Soc Am (August 2005)

500 kHz or 8.5 GHz?
And all the ranges in between.

Lock-in Amplifiers for your periodic signal measurements



Find out more

 Zurich
Instruments

Characterizing materials for superconducting radiofrequency applications—A comprehensive overview of the quadrupole resonator design and measurement capabilities

Cite as: Rev. Sci. Instrum. 92, 064710 (2021); doi: 10.1063/5.0046971

Submitted: 9 February 2021 • Accepted: 25 May 2021 •

Published Online: 16 June 2021



View Online



Export Citation



CrossMark

S. Keckert,^{1,a)}  R. Kleindienst,¹ O. Kugeler,¹  D. Tikhonov,¹  and J. Knobloch^{1,2} 

AFFILIATIONS

¹ Helmholtz-Zentrum Berlin, Hahn-Meitner-Platz 1, 14109 Berlin, Germany

² Universität Siegen, Walter-Flex-Str. 3, 57068 Siegen, Germany

^{a)} Author to whom correspondence should be addressed: sebastian.keckert@helmholtz-berlin.de

ABSTRACT

Test cavities to characterize superconductor samples are of great interest for the development of materials suitable for superconducting radio frequency (SRF) accelerator systems. They can be used to investigate fundamental SRF loss mechanisms and to study the material limitations for accelerator applications. Worldwide, this research is based on only few systems that differ in operating frequency, sample size and shape, and the accessible parameter space of frequency, temperature, and RF field strength. For useful performance predictions in future accelerators, it is important that the operating parameter range is close to that employed in accelerating systems. Since 2014, the Helmholtz-Zentrum Berlin has operated such a system built around a redesigned Quadrupole Resonator (QPR). It is based on a system originally developed at CERN. Important new design modifications were developed, along with new measurement techniques and insight into their limitations. In the meantime, an increasing number of laboratories are adopting the QPR for their measurement campaigns. This paper provides a comprehensive overview of the state-of-the-art, the wide spectrum of measurement capabilities, and a detailed analysis of measurement uncertainties, as well as the limitations one should be aware of to maximize the effectiveness of the system. In the process, we provide examples of measurements performed with Nb₃Sn and bulk niobium.

© 2021 Author(s). All article content, except where otherwise noted, is licensed under a Creative Commons Attribution (CC BY) license (<http://creativecommons.org/licenses/by/4.0/>). <https://doi.org/10.1063/5.0046971>

I. INTRODUCTION

Material properties determine and limit the performance of superconducting radio frequency (SRF) cavities, both in terms of attainable accelerating gradient and quality factor. After decades of research, superconducting cavities made from bulk niobium can be consistently produced with quality factors above 10^{10} and accelerating gradients above 30 MV/m. Beyond bulk niobium, significant improvements remain possible, however, as compound superconductors such as Nb₃Sn, NbN, and MgB₂ exist where all have higher critical temperatures (T_c) and superheating fields (H_{sh}).¹

As manufacturing cavities from bulk material are not practical for compound superconductors, thin film coatings on niobium or copper cavities present themselves as a good option. Common

techniques to assess the quality of deposited thin films, such as XRD or electron microscopy, are insufficient in determining the RF properties relevant for SRF cavities. For this, a dedicated measurement of the superconducting material properties when exposed to a high RF field is necessary. Before going through the extensive effort of developing often complex 3D cavity coating techniques, it is highly desirable to first analyze the fundamental material properties. The most promising materials and coating techniques can subsequently be applied to full cavities. Several such sample test cavities exist.^{2–6} However, most of these operate in a frequency, temperature, or RF field range that is not directly applicable to accelerating cavities.

The one design that readily can access the relevant ranges of all these parameters is the so-called Quadrupole Resonator (QPR),

whose state-of-the-art version is discussed in detail in the following. As we will see, the QPR can be an ideal tool to characterize superconducting samples in RF fields at different frequencies, in a wide range of sample temperatures and RF field strengths. A multitude of parameters is directly accessible, e.g., surface resistance, RF quench field, penetration depth, and critical temperature. Furthermore, quantities of the superconducting as well as the normal state can be derived, such as DC critical fields, energy gap, Ginzburg–Landau parameter, RRR, or normal state resistivity. However, a detailed investigation and analysis of systematic uncertainties and limitations is required to fully exploit the QPR's capabilities. In the following, we provide a comprehensive review of these aspects with measurement examples.

A. Quadrupole resonator

The QPR, originally designed at CERN in 1997,^{7–10} is shown schematically in Fig. 1. Four hollow niobium rods are suspended from the top plate of the niobium screening cylinder and are connected in pairs right above the sample surface. The whole resonator is immersed in liquid helium. A subset of the RF eigenmodes in such a geometry is strongly focused around the rods, and the resonance frequency is determined by the length L of the rods $f_0 \approx \frac{c}{2L}$ not by the dimensions of the screening cylinder. These modes subject the sample to an RF magnetic field, which is a prerequisite for all measurements described below. They have quadrupolar symmetry, hence the name quadrupole resonator. A color map of the RF magnetic field on the sample surface is provided later in Fig. 9. The flat sample is welded to a niobium tube, which is separated from the screening cylinder by a coaxial gap. RF modes below a threshold (cutoff) frequency decay exponentially in the coaxial gap, which is necessary to limit the field at the normal conducting flange connection, whose heating otherwise would lead to measurement bias. This field suppression works most efficiently for quadrupole modes, and it is therefore mandatory to avoid the excitation of lower symmetry modes in the cavity.

A heater and temperature sensors are mounted to the bottom of the sample, allowing a calorimetric measurement of the surface resistance, as described in Sec. IV A. As the sample and the resonator are thermally decoupled, measurements can be performed at arbitrary temperatures, even above 9.2 K, the critical temperature of niobium. The penetration depth of the sample material can be measured via the frequency shift observed when heating the sample. Short high power RF pulses are used to probe the RF critical field.

II. DESIGN AND PRODUCTION

The design of the quadrupole resonator has many degrees of freedom, allowing and requiring thorough RF, thermal, and mechanical simulations. The RF design places upper bounds on the maximum attainable field at which sample measurements can be performed. Thermal effects need to be considered as they are a major source of measurement bias and mechanical stability and resonances can greatly limit the attainable results in practice.

A. RF design

To measure superconducting samples with very low surface resistances at high fields, an optimal RF design would be one in

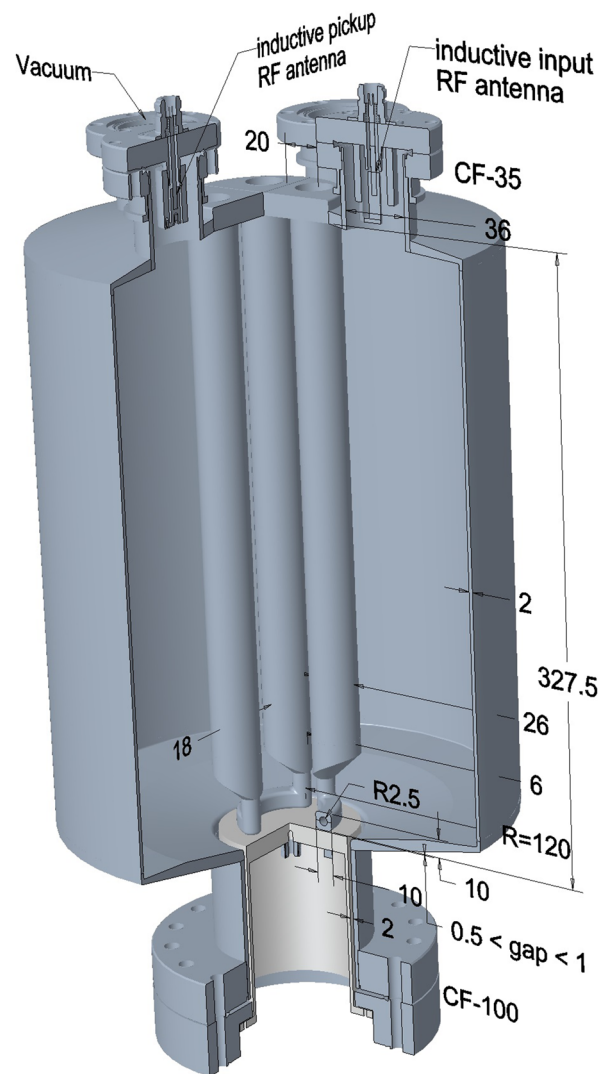


FIG. 1. Cross-sectional view of the quadrupole resonator. It consists of two pairs of hollow rods welded into a niobium cylinder at their top end and interconnected with two hollow pole shoes at their bottom end. The field antennae can be attached at four CF35 ports at the top face of the resonator, and a sample can be attached to a CF100 port underneath the rods. When operated at a quadrupole mode, the RF magnetic field is focused onto the sample underneath the pole shoes.

which the peak magnetic fields are concentrated across the sample surface, while peak magnetic and electric fields remain low on the rods and screening cylinder: This can be expressed as maximizing the peak field ratios $\hat{H}_{\text{sample}}/\hat{H}_{\text{rods}}$ and $\hat{H}_{\text{sample}}/\hat{E}_{\text{rods}}$. Increasing the magnetic field homogeneity on the sample surface $\frac{\langle H^2 \rangle_{\text{sample}}}{\hat{H}_{\text{sample}}^2}$ improves measurement resolution while reducing bias. Furthermore, the heating on the normal conducting flange at the end of the coaxial cutoff tube needs to be kept as low as possible. Here, it is useful to define a heating parameter,

$$\delta = \frac{\int_{\text{sample}} \|H\|^2 dS}{\int_{\text{flange}} \|H\|^2 dS}, \quad (1)$$

which should remain above 10^6 at any rate to accommodate the difference in surface resistance between the superconducting sample and the stainless steel flange.

An optimized geometry was reached by varying each of the geometric parameters individually and within typical boundaries allowing for mechanical tolerances.^{11,12} The radius of the niobium rods and the distance between the sample and rods were identified to be critical parameters. Increasing the radius of the rods reduced the peak electric field significantly, while decreasing the distance between the sample and the rods improved the peak magnetic field ratio, at the cost of lower field homogeneity. Whereas the heating parameter δ appears to have improved as well, it remains a major source of measurement bias especially at the higher harmonic measurements (Table I). For future experiments, it may be a good idea to lengthen the coaxial cutoff tube; for compatibility reasons with the CERN setup, this was omitted in the Helmholtz-Zentrum Berlin (HZB) design.

B. Mechanical design and production

The mechanical design of the HZB QPR is shown in Fig. 1. It deviates from the CERN design in the following points:

1. The top and bottom plates of the screening plate are inclined, allowing liquids to flow out naturally during surface treatment.
2. The niobium rods are rolled from 3 mm sheets. They are hollow to allow superfluid helium to efficiently cool RF power dissipation during operation.
3. The wall thickness of the screening cylinder was reduced to 2 mm, and a flange connection in the middle of the screening cylinder was removed. While this significantly reduced the cost of the cavity, it also decreased its mechanical stability and increased its susceptibility to microphonics.

The reduced stability leads to a high pressure sensitivity of the QPR, with $df/dP = -960$ Hz/mbar being roughly three orders of magnitude higher than for TESLA cavities.¹³ The static Lorentz force coefficient is also very high $df/dB = -0.96$ Hz/mT²—a peak magnetic field of 100 mT leading to a detuning of roughly 10 kHz. Unavoidable vibrational modes of the rods, coupled strongly to the cavity fields, pose further challenges to the RF control system, as

TABLE I. Comparison of figures of merit between the baseline and the optimized design for the first quadrupole mode. The coaxial cutoff length was increased to 86.4 mm. Earlier publications state $\delta_{\text{HZB}} = 2.1 \cdot 10^6$, which is valid for the initial cutoff length of 78.5 mm.

Parameter	Baseline design	HZB design
$\dot{H}_{\text{sample}}/\dot{H}_{\text{rods}}$	0.81	0.89
$\mu_0 \dot{H}_{\text{sample}}/\dot{E}$	4.76 mT/(MV/m)	7.69 mT/(MV/m)
$\frac{\langle H^2 \rangle_{\text{sample}}}{\dot{H}_{\text{sample}}^2}$	0.18	0.16
δ	$1.65 \cdot 10^6$	$3.8 \cdot 10^6$

further discussed in Sec. III. The QPR was manufactured by Niowave Inc., in 2014.

C. Surface treatment

After production, superconducting cavities routinely go through a series of surface finishing procedures to ensure high gradients and quality factors. The treatment performed on the QPR followed the standard procedure for high grade niobium cavities:¹⁴

- degreasing,
- 150 μm Buffered Chemical Polishing (BCP),
- high temperature 600 °C bake,
- 10 μm light BCP,
- rinse to resistivity in ultrapure water (18M Ω cm),
- high pressure rinse,
- low temperature 120 °C bake.

Even though the quadrupole resonator differs significantly from the elliptical cavities for which these procedures have been optimized for, all procedures could be performed with minor tooling adaptations and without significant issues. Note that the removal rate during the etching process is dependent strongly on the acid flow rate, which is significantly higher around the rods and loops compared to the outside of the screening cylinder. As an ultrasonic device for measuring the material removal during the procedure can only be placed on the outer wall, one must be aware that more material is actually being removed from the rods and loops. As the distance between the rods and sample strongly affects the calibration constant defined in Eq. (3), it was explicitly remeasured after the BCP using an indium crush test.

III. DIAGNOSTICS AND OPERATION

The QPR sample is top-hat-shaped, a sketch is shown in Fig. 2. For testing operation, it is inserted into the sample port of the resonator from below and attached vacuum-tight. Its top surface is

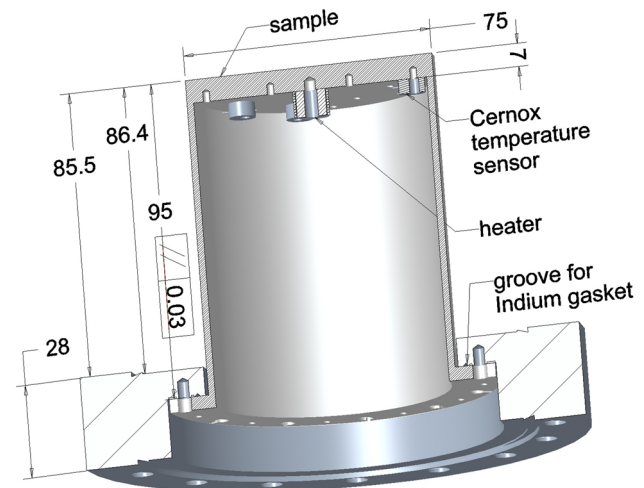


FIG. 2. Modified sample chamber and adapter flange. A heater is positioned axially underneath the face of the sample. Cernox temperature sensors are mounted at dedicated positions around the heater.

covered with (or made of) the actual material to be tested. It serves as the actual sample and is exposed to the RF field generated in the resonator chamber, with the maximum RF magnetic fields occurring immediately underneath the pole shoes. The sample's outer cylindrical surface, when brought into place, acts as an inner conductor of a coaxial line, reducing RF leakage out of the sample port of the resonator. Hence, the entire sample chamber assembly is an active part of the resonator and has to be treated similar to the cavity regarding surface quality, cleanliness, and manufacturing tolerances.

The sample design was devised with the desire to avoid a welding step anywhere along the sample preparation procedure, in particular subsequent to the application of a coating procedure of a possibly temperature sensitive SRF film. In this design, the Nb cylinder is separable from the double-sided CF100 flange, which is in turn attached to the resonator. This was implemented by preparing sample cylinders with a Nb flange welded to their bottom, which can be mounted on a matching flange machined into the CF100 using an indium gasket. The sample chamber is closed from below by a blank flange hosting multipin feedthroughs and a dedicated pumping line (not depicted in Figs. 1 and 2).

The double sided CF100 flange is manufactured such that the sample surface is positioned immediately underneath the pole shoes, with the gap distance ranging between 0.5 and 1 mm. This gap is the most critical parameter of the entire QPR. Positive height adjustment (i.e., bringing the sample closer to the pole shoes) of the sample chamber is possible by machining the flange, which might be necessary after repeated steps of sample etching or polishing. Negative height adjustment and to some extent tilt adjustment are possible by copper spacers that can be placed between the sample flange and double-sided CF100 flange. After mounting the sample chamber into the resonator, the actual gap between the sample surface and pole shoes is calculated from the measured frequency of the first quadrupole mode.¹²

A small sawtooth-shaped groove was worked into the CF-100 flange to serve as a fixture for an indium wire that is placed within prior to attaching the sample. The indium wire serves as a vacuum seal and thermal and electrical contact between the sample and flange. A good thermal contact ensures sufficient heat removal from the sample and helps us to obtain a well-defined temperature reference point at the sample chamber bottom with respect to the heated sample top to enable a calorimetric measurement. Indium remnants on the niobium part after disassembly, if needed, can be easily dissolved by etching with dilute hydrochloric or nitric acid. Having one detachable part of high purity niobium enables contamination critical procedures, such as heat treatment in UHV furnaces, e.g., for diffusion coating with Nb₃Sn or nitrogen doing/infusion.

The flat bottom of the sample is equipped with threaded holes (M2.5 and M4) for mounting diagnostics and a heater. In addition, the bottom part of the sample chamber can be used to host additional diagnostics.

The DC heater ($R \approx 50\Omega$) for active control of the sample consists of a nichrome wire wrapped around a copper rod. Nichrome is a non-magnetic alloy with high resistivity at cryogenic temperatures. The thermal contact to the copper rod is enhanced by the indium foil and epoxy glue. A twisted pair of cables is used to eliminate DC magnetic fields generated by the heater current. This is crucial since

systematic studies on trapped magnetic flux, thermocurrents, and cooldown dynamics require active heating during the superconducting transition. For temperature measurements, calibrated Cernox sensors are used (CX-1030-CU-1.4L, Lake Shore Cryotronics). Sensors are attached with M2.5 titanium screws through the clearance hole to the sample. All diagnostics and screws are ferromagnetic free. Heater and temperature sensors are powered by an LS336 controller. The DC heater power is measured using two digital multimeters (see Sec. IV C 1 for details).

The QPR is operated in a vertical liquid helium bath cryostat. Due to the coaxial design of the sample chamber and resonator bottom, the sample is thermally decoupled from the resonator since the direct thermal contact only exists at the CF100 flange, which is also in direct contact with the liquid helium bath. The cryostat pressure is actively stabilized (typically $\pm 60\ \mu\text{bar}$), and the bath temperature is kept constant at all times (typically 1.8 K), while arbitrary sample temperatures above the bath temperature can be selected using the DC sample heater. The cryostat is equipped with two magnetic shields, suppressing the earth magnetic field to $<1\ \mu\text{T}$ at cryogenic temperatures.¹²

In the RF system, a phase locked loop is used to operate the QPR at stable RF field.¹² The low-level RF system is made broadband to cover the frequency range of 400 MHz up to 1.3 GHz with minor adaptations only.¹⁵ For each quadrupole mode, dedicated power amplifiers and circulators are available.

During operation, dealing with microphonics has been a major challenge. Figure 3 shows the detuning of the operational quadrupole mode—peak to peak; the resonance frequency is shifted by several 100 Hz, which needs to be compensated for by the RF control system. This is similar to the bandwidth of the resonator of about 340 Hz, given by the strongly coupled input antenna. The dominant frequency component in the detuning spectrum is found at approximately 100 Hz. This frequency corresponds to several vibrational modes of the niobium rods, which may be excited by pumps or other external sources.^{12,16} Modulations of the RF power source may also couple to these vibrational modes and must therefore be diligently suppressed.

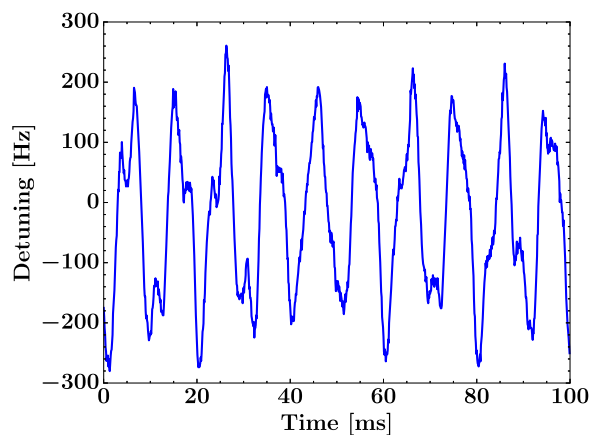


FIG. 3. Detuning of the first quadrupole mode shown in the time domain.

IV. MEASURING RF SURFACE RESISTANCE

The main purpose of the QPR is to perform precision measurements of the RF surface resistance at different frequencies and as a function of temperature and RF field strength. The comparatively low frequency of the first quadrupole mode provides high sensitivity to residual resistance at low sample temperature since the BCS resistance is very low. This aspect is difficult to access with other sample test systems, which generally must operate at higher frequency where the BCS resistance tends to dominate. Furthermore, the surface resistance is measured with a calorimetric compensation technique enabling absolute measurements without the need for cross-calibration to a reference sample. The thermal decoupling of the sample assembly and surrounding resonator allows for measurements in a wide range of temperatures that can be adjusted quickly. This is important to directly distinguish between the residual resistance and temperature-dependent BCS resistance.

A. Calorimetric measurement technique

The calorimetric measurement principle uses an RF-DC compensation technique consisting of three steps:

1. Without the RF field, the sample is heated to the temperature of interest. In thermal equilibrium, the required heater power is recorded using a four-wire setup (P_{DC1}).
2. The RF is switched on to the power level of interest, and a proportional-integral-differential (PID) control loop reduces the heater power to stabilize the temperature of interest again (P_{DC2}).
3. Once thermal equilibrium is reached, the RF dissipated power is given by the difference in heater power $P_{diss} = \Delta P_{DC} = P_{DC1} - P_{DC2}$.

The average surface resistance is then given by

$$R_S = \frac{2P_{diss}}{\int_{\text{sample}} \|H\|^2 dS} = 2c_1 \frac{\Delta P_{DC}}{\hat{H}_{\text{sample}}^2}, \quad (2)$$

with the RF calibration constant

$$c_1 = \frac{\hat{H}_{\text{sample}}^2}{\int_{\text{sample}} \|H\|^2 dS}. \quad (3)$$

As usual for cavity measurements, the peak RF magnetic field on the sample \hat{H}_{sample} is derived from the measured RF power level at the pickup antenna P_t . The calibration constant c_1 for each quadrupole mode is obtained from simulations¹² and corrected for the actual gap distance between the sample surface and pole shoes.¹⁵

Obviously, the surface resistance measurement is restricted to a regime where $P_{diss} < P_{DC1}$. To increase the measurable RF field range, pulsed RF power is used. For standard operation, a pulse period of 133 ms and duty factors down to 30% are used, providing reliable results. This choice of pulse repetition rate prevents excitation of microphonics by Lorentz force detuning at the dominant mechanical modes near 100 Hz.

B. Experimental results and measurement limitations

The QPR has already been used to characterize various samples, materials, and surface preparation techniques such as bulk

niobium,^{12,15,17} Nb coated on copper,¹⁸ Nb₃Sn,^{15,19,20} and NbTiN coatings, including an S-I-S' multilayer structure.^{15,18,21} In the following, two exemplary datasets are presented, obtained from a bulk niobium sample and a thick film of Nb₃Sn on niobium.

1. Nb₃Sn sample

A Nb₃Sn sample was prepared at Cornell University using the coating procedure commonly applied to single cell cavities.²² For a detailed analysis of this sample, see Ref. 15, and the critical field measurement was published in Ref. 19.

Surface resistance data are available for temperatures in the range of 2–10 K and RF fields of 10–70 mT, limited at high field by RF heating. Measurements were restricted to the first two quadrupole modes at frequencies of 414 and 846 MHz due to instrumentation issues at that time. A TESLA-shaped elliptical cavity would need to be operated at $E_{acc} = 2.3$ –16.4 MV/m to achieve the same peak magnetic fields.¹³ Similar maximum accelerating fields were achieved with Nb₃Sn coated cavities.²³ Note that the Nb₃Sn coating covers all exterior surfaces of the sample chamber. For that reason, RF losses on the sidewall of the sample are negligible and do not cause any bias in surface resistance measurements at high temperature, assuming a high-quality film on the sidewall.

Exploring the parameter space of the sample temperature and RF field strength, the surface resistance was measured in datasets of varying RF field at constant temperature each. This is more time efficient than varying the temperature at constant RF field since after every change in sample temperature the reference heater power has to be recorded after a steady state has been reached. During post-processing, $R_S(T)$ curves are extracted for each value of the RF field.

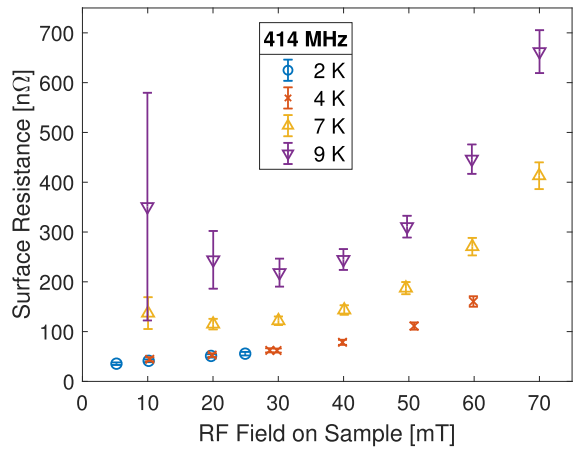
Figure 4 shows exemplary curves of surface resistance vs RF field, which also present the measurement limitations for that sample: Toward the low RF field, the measurement uncertainty increases due to the small relative change of DC heater power (see also Sec. IV C 4). This especially impacts the data analysis of $R_S(T)$ at 10 mT toward increasing temperature despite the fact that the BCS surface resistance is significantly higher. The maximum RF field accessible at a given sample temperature is limited by RF heating, i.e., the surface resistance. Note that at high temperature, an increasing range of RF field can be accessible, even though R_S increases strongly with temperature. Analyzing $R_S(T)$, heating limits the minimum temperature on each curve since the RF field level is kept constant. The impact of high surface resistance is especially visible at 846 MHz: At 50 mT, data are available above 5 K only, which results in only few points on this $R_S(T)$ curve. In that case, BCS fits have non-negligible uncertainties due to the very limited number of data points.

2. Bulk niobium sample

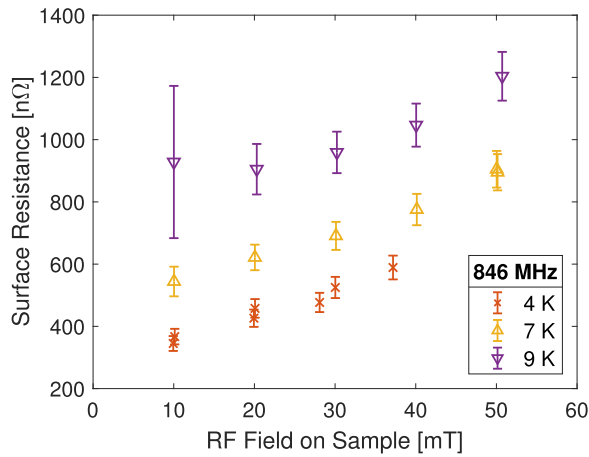
A bulk niobium sample was characterized at 414 and 846 MHz. For each $R_S(T)$ curve, the BCS approximation

$$R_S(T) = \frac{a}{T} \left(\frac{f}{414\text{MHz}} \right)^2 \exp\left(-\frac{\Delta}{k_B T}\right) + R_{\text{res}} \quad (4)$$

is used to extract the residual resistance R_{res} , BCS scattering parameter a , and superconducting energy gap Δ . Note that a is normalized to the first quadrupole mode frequency. We neglected the



(a)

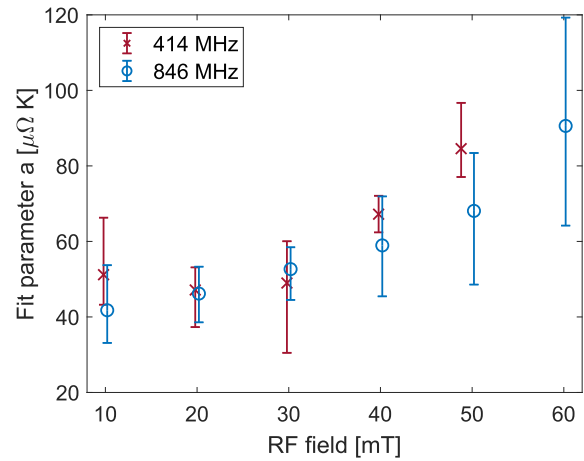


(b)

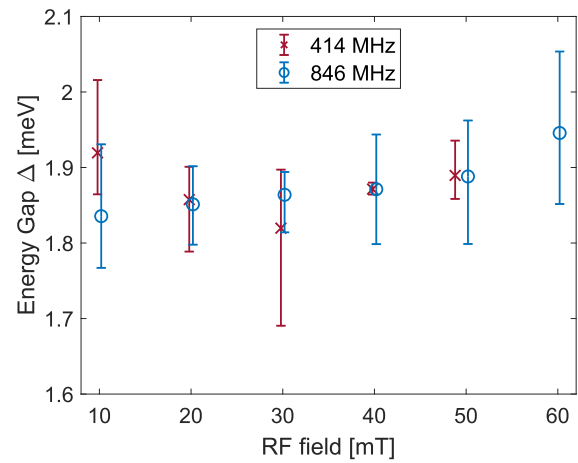
FIG. 4. R_S of Nb_3Sn vs RF field at (a) 414 and (b) 846 MHz. Measurements toward higher fields are limited by RF heating. At low field, the uncertainty increases with temperature due to the small relative change in heater power.

weak frequency dependence of a since the deviation of Eq. (4) from the full BCS calculation in Refs. 24 and 25 is less than 1.3% for frequencies of 0.4 up to 1.3 GHz. Figure 5 shows the resulting parameters for both measurement frequencies as a function of RF field. Fit data are available at integer multiples of 10 mT, and error bars show the overall measurement and fit uncertainty.

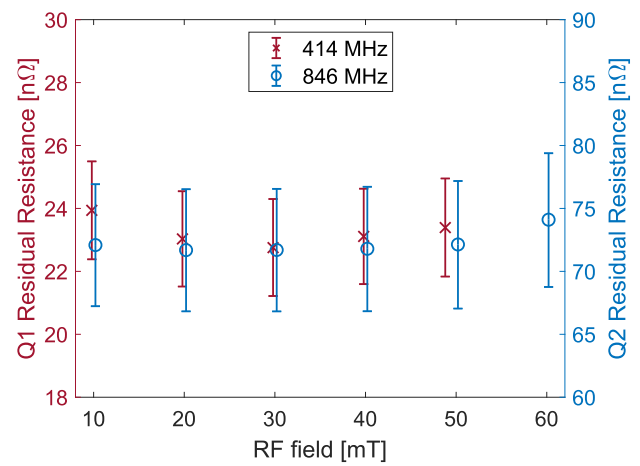
After subtracting RF field independent residual resistance values of 23 and 73 nΩ for 414 and 846 MHz, respectively, from measurement data, the temperature dependent BCS resistance is shown as a function of RF field in Fig. 6. At low fields of 10 and 20 mT, the data perfectly match the expectation of $B_{BCS} \propto f^2$. Correspondingly, this excludes significant frequency specific systematic errors of the RF measurement system. Toward the higher RF field, the increase in R_{BCS} is suppressed at higher frequency. Note that systematic errors due to losses in the coaxial structure may affect the Q-slope behavior and also depend on frequency (see Sec. IV C). Comparing the



(a)



(b)



(c)

FIG. 5. Bulk Nb BCS fit results vs RF field at 414 and 846 MHz showing the (a) scattering factor, (b) energy gap, and (c) residual resistance. The error bars show the overall measurement and fit uncertainty.

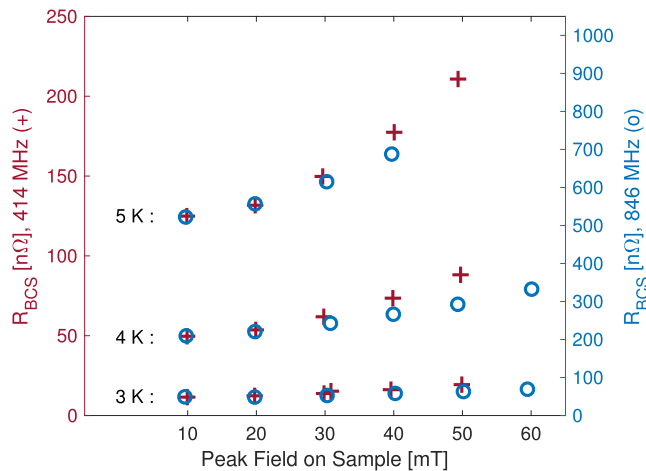


FIG. 6. Temperature dependent BCS surface resistance vs RF field for a bulk Nb sample after subtracting RF field independent R_{res} of 23 and 73 n Ω for 414 and 846 MHz, respectively [see Fig. 5(c)]. The ordinates are linked by $(846/414)^2 \approx 4.2$, i.e., a quadratic frequency dependence would yield perfectly overlapping curves.

observed rise of R_{BCS} to the fit parameters in Figs. 5(a) and 5(b), this can be consistently attributed to the scattering parameter a . The obtained Δ values are compatible with a mean of 1.87 meV that is independent of the RF field and frequency. Such a behavior of a agrees with empirical extensions of the BCS model of Eq. (4), introducing a polynomial dependence on the RF field in order to describe the non-linear BCS effects and medium-field Q-slope.²⁶ Note that from the literature a lower value of $\Delta = 1.5$ meV is expected.²⁷

The residual resistance is nearly independent of the RF field for both frequencies [see Fig. 5(c)]. Assuming a field independent scaling factor of $73/23 \approx 3.2$ corresponds to a frequency dependence of $R_{\text{res}} \propto f^{1.63}$. Similar scaling has been observed before on multi-mode test cavities and seems to be typical for bulk niobium.^{28,29} Note that the fit uncertainty given by error bars in Fig. 5(c) is dominated by the systematic RF measurement uncertainty of 9.2% (see Sec. IV C 4). This is mainly relevant when comparing different frequencies since RF calibration errors systematically shift the entire dataset obtained at one quadrupole mode. In the case of the scattering parameter a , the statistical uncertainty of the fit is larger than the RF measurement uncertainty, while the energy gap Δ is independent of such systematic shifts. For a detailed discussion how measurement errors impact BCS fit parameters, see Ref. 30.

C. Resolution, accuracy, and precision

The surface resistance measurement uncertainty depends on properties of the sample such as its thermal conductivity and the surface resistance itself. For that reason, no universally applicable quantitative analysis can be provided. However, the thermal conductivity of the sample chamber assembly is dominated by the stainless steel bottom flange. Up to now, all bulk niobium samples did not show significant differences in their thermal behavior. For that reason, a summary is given in Table II, based on realistic assumptions as discussed in the further course of this section. For a detailed analysis, the reader is referred to Ref. 15.

TABLE II. Summary of surface resistance measurement uncertainties and limitations.

Quantity	Value
Typical accuracy of R_S w/o bias	9.2%
Minimum resolvable R_S	0.5 n Ω at $\mu_0 H_{\text{RF}} = 10$ mT in general: 50 n Ω (mT) ²
Systematic bias of R_S at Q3	>25 n Ω
Systematic uncertainty of R_S due to temperature gradients	<1%
Calorimetric accuracy of heater power measurement	<0.3%
Minimum RF field level	5 mT
Accuracy of H_{RF}	6.5%
Vertical ΔT between the RF surface and temperature sensor	<5 mK

1. Calorimetric accuracy and temperature stability

A LakeShore LS336 device is the central unit of the calorimetric measurement, reading out up to four temperature sensors and powering the DC heater. The output of the internal PID controller is a variable current source with 16-bit digital resolution. In the worst case, one bit of the DAC corresponds to a current step of 30.5 μA or a 47 nW step in heater power at a load resistance of 50 Ω . The RMS noise of the current source of 0.12 μA is negligible.

The DC heater power is obtained from a four-wire measurement. Hence, systematic errors from a temperature dependent resistance are excluded and insulation failures can be detected.

The heater voltage is measured with an HP 34401A multimeter having a worst-case accuracy of better than 660 μV . This is below the step size defined by the current source $V_{\text{step}} = 50\Omega \cdot 30.5 \mu\text{A} = 1.5$ mV and hence no limitation of the measurement system. However, voltage noise coming from the electromagnetic interference may disturb the voltage measurement.

The heater current is measured with a Keithley 2100 multimeter. It has a resolution of at least 1 μA , which is significantly better than the D/A resolution of the current source. The accuracy of the device limits the overall current accuracy to about 0.3% in the worst case.

For sample temperatures up to 20 K, the PID controlled heater provides temperature stability better than 1 mK, typically close to the resolution limit of 0.1 mK. The temperature accuracy is set by the calibration accuracy of the respective temperature sensors. In terms of Cernox[®] sensors, this is ± 5 mK for temperatures below 10 K, increasing up to ± 9 mK at 20 K.

2. Gradients of temperature and RF field

The RF-DC compensation technique for surface resistance measurements relies on the assumption that any RF dissipation on the sample surface leads to the same thermal response as the exact same amount of DC heater power. As discussed below (see Sec. IV C 6), this assumption is violated e.g., by RF heating of additional parts of the sample chamber like the bottom flange. However, this effect can be suppressed by using a superconducting material on all parts of the sample chamber and copper coating on the flange.

Another source of systematic error comes from asymmetries in sample heating and temperature gradients on the sample “disk.” By construction, the PID controller relies on one temperature sensor at the bottom surface. However, the lateral distributions of heating (RF vs DC) differ. This intrinsic property of the QPR is studied with a thermal simulation.¹⁵ The DC heater (diameter 10 mm) is placed in the center of the sample bottom surface. For RF dissipation, the squared magnetic field on the sample surface is used as a boundary heat source. Exemplary horizontal temperature profiles for 50 mW of heating power (RF or DC) are shown in Fig. 7.

Comparing the scenarios of DC heating and RF heating in the high-field region yields a temperature response at the reference sensor location ($r = 24.1$ mm) that is very similar [see Fig. 7(b)]. The deviation of 0.5 mK is close to the resolution limit of the temperature sensor ($\Delta T = 0.1$ mK). For the low field region, a deviation of

−2.5 mK is observed. This justifies the assumption of RF-DC compensation in case the sensor is mounted below a high-field region. The curves for RF heating shown in Fig. 7 correspond to the maximum RF field, representing a worst-case scenario. Lower RF fields yield intermediate results with a less temperature difference at the reference location.

The vertical temperature gradient across the thickness of the sample is shown in Fig. 8 for DC and RF heating. The difference between DC and RF heating is less than 5 mK for sample temperatures below 6 K and hence negligible. In the case of a bulk niobium sample (RRR 300), this vertical temperature difference would yield a systematic underestimation of the true surface resistance on the permille level.

A potentially significant mismatch of measured values for R_S and H_{RF} arises from field-dependent surface resistance (Q-slope). Furthermore, in the case of a nitrogen doped sample, where the surface resistance decreases with increasing B_{RF} over a certain range, the field level of minimum surface resistance is shifted systematically^{12,31} due to the fact that the RF field is inhomogeneous across the sample.

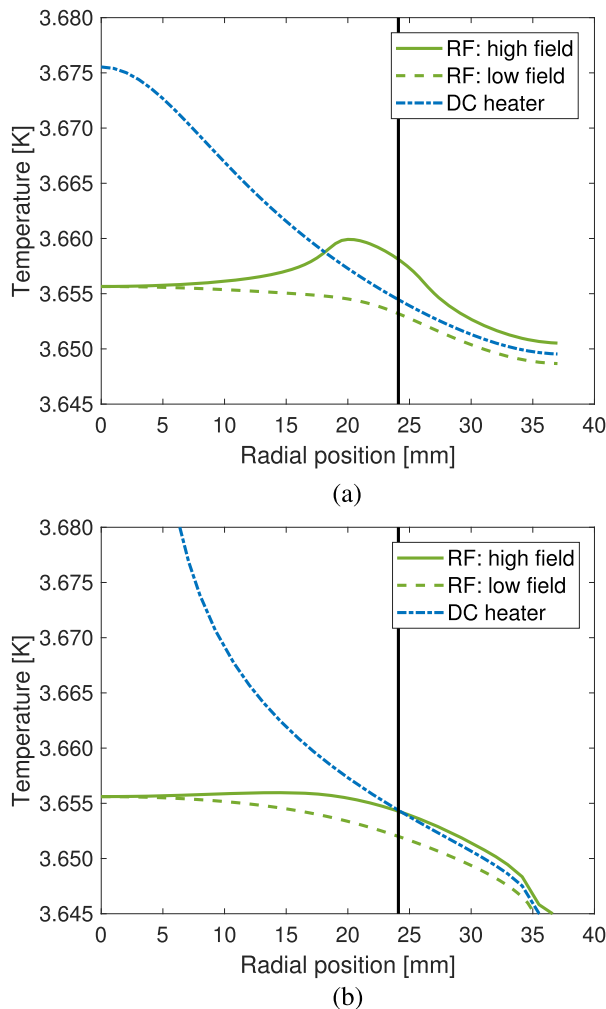


FIG. 7. Exemplary simulation results for 50 mW of heater power applied to the different boundary heat sources individually. The temperature profiles are shown for (a) the RF surface and (b) the sample bottom where the temperature sensor is mounted. The radial position of the temperature sensor is indicated by a vertical black line.

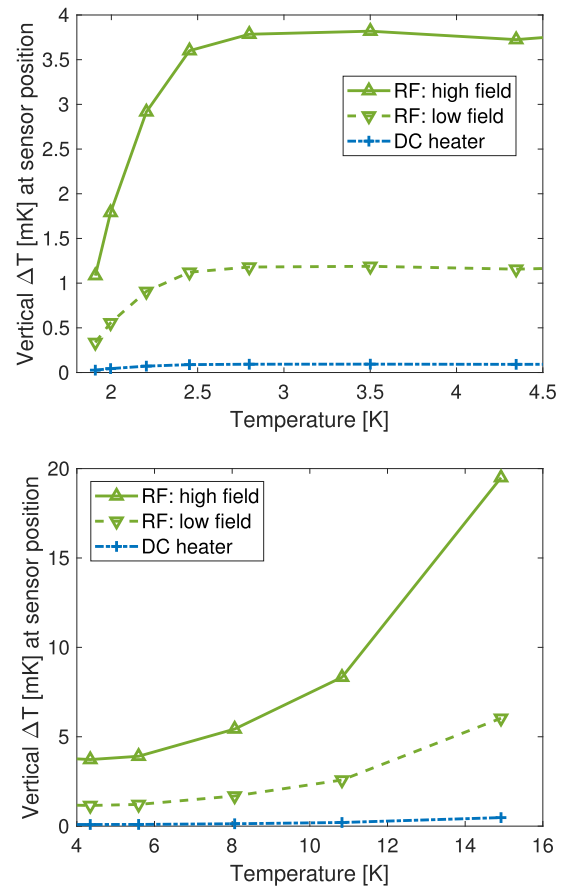


FIG. 8. Vertical temperature gradient $\Delta T = T_{\text{top}} - T_{\text{sensor}}$ at the location of the reference sensor. “Low field” and “high field” denote the cases of mounting the sensor on the same radius but below the location of lowest respectively highest RF field.

However, the RF field profile on the sample is known from simulations, enabling numerical methods that correct for such effects in the offline data analysis.^{12,32} A color map of the RF field on the sample is shown in Fig. 9. Note that in any case, the lateral uniformity of R_S is required. Localized heating, e.g., by defects or multipacting, can hardly be investigated.

3. Helium-bath stability

The pressure stability of the liquid helium bath has an influence on the heater power and hence the thermometry precision. Measurements show that the pressure fluctuations of the vertical bath cryostat depend on the helium level inside the bath cryostat, ranging from ± 40 up to ± 80 μ bar. At the operating temperature of 1.8 K, this corresponds to fluctuations of a sample temperature of ± 0.6 mK.¹⁵

During R_S measurements, the sample temperature is actively controlled, which transforms temperature changes in the LHe bath into heater power changes ΔP_{heater} . Using a thermal simulation of the sample chamber system leads to ΔP_{heater} on the order of 20 μ W. Obviously, this error source limits the entire setup at sample temperatures that are very close to the helium bath temperature. For $T \gtrsim 1.825$ K, the resulting error is less than 6%, quickly dropping with increasing temperature. This impact can be suppressed further by using a sufficiently long averaging dataset of several minutes.

4. RF measurement accuracy and overall surface resistance accuracy

The RF power measurement accuracy contributes significantly to the overall R_S accuracy. Keysight U2042XA power meters are used with an accuracy of ± 0.18 dB or $\pm 4.1\%$ for all relevant frequencies and power levels. Approximately 0.2 dB have to be added due to the uncertainty of RF cable losses, yielding an overall RF power measurement uncertainty of 0.4 dB or 9.2%, in the following denoted as $\frac{\sigma_{\text{RF}}}{\text{RF}}$.

Using Eq. (2), the propagation of uncertainties yields the relative error

$$\left(\frac{\sigma_{R_S}}{R_S}\right)^2 = 2\left(\frac{\sigma_{P_{\text{DC}}}}{\Delta P_{\text{DC}}}\right)^2 + \frac{1}{2}\left(\frac{\sigma_{\text{RF}}}{\text{RF}}\right)^2, \quad (5)$$

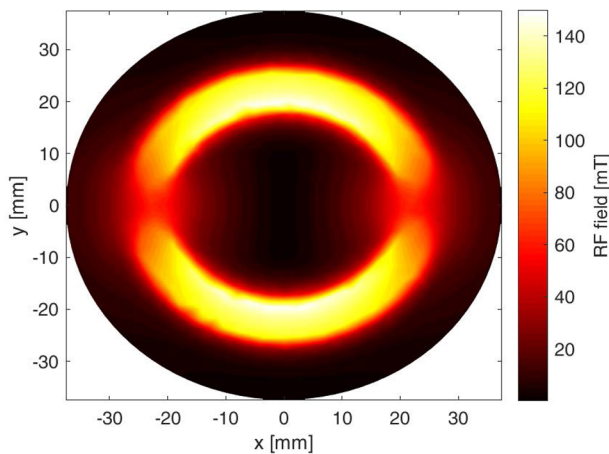


FIG. 9. RF magnetic field on the sample surface at the first quadrupole mode. At higher harmonic quadrupole modes, the magnetic field on the sample changes only very little, which would not be visible in this representation.

assuming

$$\frac{\sigma_{Q_t}}{Q_t} = \frac{\sigma_{P_t}}{P_t} = \frac{\sigma_{\text{RF}}}{\text{RF}} = 9.2\%. \quad (6)$$

For the RF field, we obtain

$$\left(\frac{\sigma_B}{B}\right)^2 = \left(\frac{\sigma_{Q_t}}{2Q_t}\right)^2 + \left(\frac{\sigma_{P_t}}{2P_t}\right)^2 = \frac{1}{2}\left(\frac{\sigma_{\text{RF}}}{\text{RF}}\right)^2 \quad (7)$$

and hence

$$\frac{\sigma_B}{B} = \frac{1}{\sqrt{2}} \cdot 9.2\% = 6.5\%. \quad (8)$$

Note that for σ_{R_S} , the heater power uncertainty $\sigma_{P_{\text{DC}}}$ is normalized to the difference $\Delta P_{\text{DC}} = P_{\text{diss}}$. This is important for measuring R_S at low field or at high temperature where $\frac{\sigma_{P_{\text{DC}}}}{\Delta P_{\text{DC}}} = \frac{\sigma_{P_{\text{DC}}}}{P_{\text{diss}}}$ can become very large. Restricting the useful measurement range to $\sqrt{2} \frac{\sigma_{P_{\text{DC}}}}{\Delta P_{\text{DC}}} \leq \frac{1}{\sqrt{2}} \frac{\sigma_{\text{RF}}}{\text{RF}}$ sets a lower boundary on ΔP_{DC} and hence P_{diss} . Depending on the actual surface resistance, this translates into a minimum RF field required for this measurement. For RRR 300 niobium with $R_{\text{res}} = 5$ n Ω , a value of typically 5 mT is obtained.

5. Minimum resolvable surface resistance

At very low temperature, where the BCS resistance is negligible, the resolvable surface resistance sets a limit on the minimum residual resistance that can be measured. Fitting data for $R_S(T)$ might yield a lower R_{res} ; however, deviations from the implied theoretical model cannot be resolved in that case. At sample temperatures close to the helium bath temperature, measurements are not limited by the smallest resolvable change in heater power—as that would only be 47 nW and hence correspond to an incredibly low surface resistance—but by the equivalent heater power change due to helium pressure fluctuations. Close to the helium bath temperature, $\Delta P_{\text{heater}} \approx 12$ μ W yields $R_S = 0.5$ n Ω at $\mu_0 H = 10$ mT [see Eq. (2)]. This value decreases quadratically with the RF field to ultimately $R_S = 0.003$ n Ω at the QPR quench limit of $\mu_0 H = 120$ mT. In general, the resolution parameter

$$R_{S,\text{min}} \mu_0^2 H^2 = 2 c_1 \mu_0^2 \Delta P_{\text{DC},\text{min}} = 50 \text{ n}\Omega (\text{mT})^2 \quad (9)$$

can be defined. These values apply to the first quadrupole mode, and for higher harmonic modes, the minimum resolvable surface resistance increases by about 20% due to c_1 increasing with frequency. Note that only the RF contribution via c_1 is an intrinsic property of the resonator. The resolution can be improved by decreasing the thermal conductivity of the sample chamber assembly, which reduces the DC heater power that is required to compensate temperature fluctuations caused by the liquid helium bath. However, the low thermal conductivity leads to low $P_{\text{DC}1}$, limiting R_S measurements at high RF fields due to heating.

6. Systematic bias due to parasitic losses

In the calorimetric RF-DC compensation technique, all RF losses occurring on the sample chamber are interpreted as surface resistance of the sample. Hence, parasitic losses lead to a systematically overestimated R_S . Up to now, the lowest surface resistance measured with the QPR at HZB was 8 n Ω at 2.25 K and the first quadrupole mode on a RRR 300 bulk niobium sample.¹² At the third

quadrupole mode, inconsistent data have been observed, which we attribute to insufficient damping of the RF field in the coaxial structure of the sample chamber, resulting in high parasitic losses at the bottom stainless-steel flange.

Using a combined electro-magnetic/thermal simulation workflow, the calorimetric compensation is reproduced, allowing one to estimate this systematic error.¹⁵ In terms of RF dissipation, the sample chamber is divided into three domains: sample surface, coaxial wall, and bottom flange. Using the eigenmode solver in CST MWS, RF fields inside the QPR are simulated and the damping coefficient δ_i [see Eq. (1)] is evaluated for each domain and each quadrupole mode, where the surface integral in the denominator is taken of the domain i . The dissipated power in each domain is given by

$$P_i = \frac{1}{\delta_i} \frac{R_i}{R_{\text{sample}}} P_{\text{sample}} = \frac{\gamma_i}{R_{\text{sample}}} P_{\text{sample}}, \quad (10)$$

introducing the loss coefficient $\gamma_i = \frac{R_i}{\delta_i}$. R_i denotes the surface resistance of a domain.

In general, the impact of parasitic losses on the measured R_S depends on the sample material, temperature, and RF field strength. The necessary $R_S(T)$ is calculated using the numerical BCS code SRIMP³⁴ for niobium with RRR 300 and $R_{\text{res}} = 10 \text{ n}\Omega$. The surface resistance of stainless steel is assumed to be independent of temperature (see Table III). For the surface resistance accuracy, the worst case occurs if all heating comes from RF dissipation; hence, the DC heater is off and $\Delta P_{\text{DC}} = P_{\text{diss}} = P_{\text{DC1}}$, corresponding to the maximum CW RF field at a given temperature. In the following, the RF field is set to 85% of the maximum possible value, representing a typical scenario.

Figure 10 shows the resulting ratio of dissipated power at the flange to the power dissipated in the sample. Compared to P_{flange} , the contribution of the coaxial wall can be neglected: Assuming non-ideal niobium with ten times higher residual resistance yields $\frac{P_{\text{coax}}}{P_{\text{sample}}} = 5\%$ at low temperature, further decreasing to 0.5% in the regime of dominating BCS losses.

The loss coefficient γ_i as defined above is given in units of resistance (or $\text{n}\Omega$) and seems to give a resistance contribution. However, this provides only a rough estimate since the RF-DC compensation technique cannot measure RF dissipation directly but compares power levels at constant temperature. Hence, the temperature rise or the distortion of the temperature distribution on the sample chamber has to be evaluated, which then yields the surface resistance contribution. In order to do so, a thermal simulation of the sample chamber is set up modeling all data acquisition steps. The

TABLE III. RF parameters describing the additional losses on the coaxial wall and bottom flange. For R_S of stainless steel, $\sigma_{\text{cryo}} = 2 \cdot 10^6 (\Omega\text{m})^{-1}$ and the normal skin effect is assumed.³³

	Q1 (433 MHz)	Q2 (866 MHz)	Q3 (1315 MHz)
δ_{coax}	202	206	211
δ_{flange}	$3.8 \cdot 10^6$	$2.7 \cdot 10^6$	$1.5 \cdot 10^6$
$R_{S,\text{SS304}}$	29 $\text{m}\Omega$	41 $\text{m}\Omega$	51 $\text{m}\Omega$
γ_{flange}	7.6 $\text{n}\Omega$	15 $\text{n}\Omega$	34 $\text{n}\Omega$

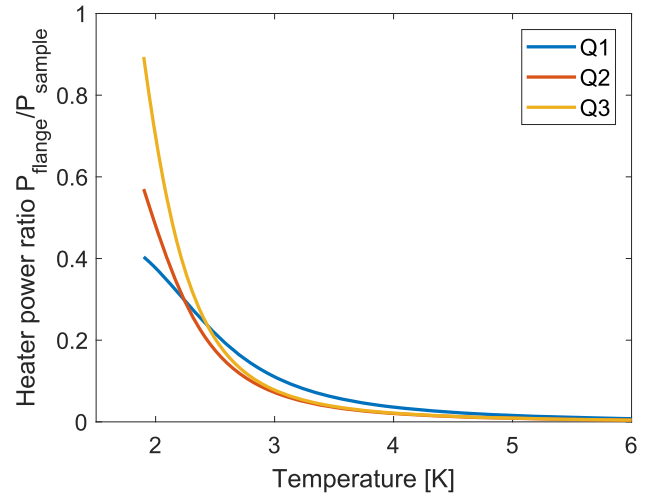


FIG. 10. Ratio of RF dissipation on the normal conducting bottom flange and a niobium sample with $R_{\text{res}} = 10 \text{ n}\Omega$.

resonator itself does not have to be taken into account since the sample chamber and resonator are thermally decoupled.

Figure 11 shows the resulting systematic overestimation of R_S . For temperatures above 4.5 K, increasing numerical noise is observed, especially at high frequency. This is due to the steep increase in BCS surface resistance on the sample surface and hence the vanishing power ratio of flange heating to sample heating (see Fig. 10). Then, the impact of ΔR_S gets negligible since $\Delta R/R$ decreases below the overall measurement accuracy. Counter-intuitively, the normal conducting flange with a surface resistance independent of temperature and RF field does not only contribute as additional residual resistance but may also impact the BCS behavior of the measured R_S .

In order to suppress this significant systematic error, the surface resistance of the bottom flange has to be reduced. Options might be

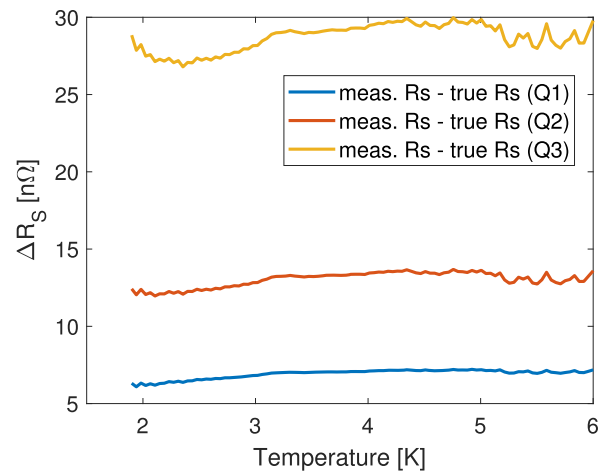


FIG. 11. Systematic errors in R_S for a RRR 300 niobium sample with $R_{\text{res}} = 10 \text{ n}\Omega$.

a copper or superconductor coating of the areas exposed to RF or even the use of a bulk superconducting flange. The surface quality of the sample chamber's cylindrical wall seems manageable in the case of niobium samples. However, additional complications arise for multilayer coatings and measurements at high temperatures: Depending on the coating setup and the used technique, high quality coatings of the sidewalls are complicated if not impossible. In this case, the substrate—typically bulk niobium—will cause a temperature dependent increase in R_S and impede measurements above 9.25 K.

V. MEASURING RF PENETRATION DEPTH

Heating up a superconductor close to its critical temperature leads to an increasing penetration depth $\lambda(T) \approx \lambda_0/\sqrt{1 - (T/T_c)^4}$. In general, this is equivalent to an increasing magnetic volume with the corresponding change in resonant frequency $\Delta f < 0$. For the QPR, the sample can be heated separately, leading to a shift in resonant frequency only due to the penetration depth of the RF sample surface,

$$\Delta\lambda = \lambda(T) - \lambda_0 = -\frac{G}{\pi\mu f_0^2} \Delta f, \quad (11)$$

with λ_0 and f_0 representing the approximately temperature independent values at low temperature. The geometry factor G is given by the RF sample surface only,

$$G = \frac{\omega\mu_0 \int_{\text{QPR}} |H|^2 dV}{\int_{\text{Sample}} |H|^2 dS}, \quad (12)$$

and is computed with electromagnetic simulations. For quadrupole modes, G increases approximately linear with frequency.

Note that the resonator is kept at constant temperature throughout the entire measurement, stabilized by the superfluid LHe bath at typically 1.8 K. The maximum expected frequency shift is $|\Delta f| \approx 1, \dots, 20$ kHz. However, its measurement is disturbed by the superimposed microphonics and changes in environmental pressure. The decreasing liquid helium level of the bath cryostat leads to a drift of center frequency of about -1 kHz/h, which has to be corrected in the data analysis. Pressure fluctuations coming from the cryogenic system cause frequency fluctuations of about ± 50 Hz on the timescale of 1 min. For that reason, careful averaging is required, which also suppresses microphonic detuning.

An automated setup using a computer controlled vector network analyzer (VNA, Agilent E8358A) is used for measurements.¹⁵ This enables data acquisition at multiple resonant modes during one thermal cycle. Exemplary measurement data for a bulk niobium sample are shown in Fig. 12, together with fits according to Eq. (11). Reference points at low temperature before and after the thermal cycle are used to derive the pressure sensitivity of each mode and to correct the systematic drift due to the decreasing level of liquid helium. Values for critical temperature (T_c) and penetration depth at 0 K are obtained from non-linear fits using Eq. (11). For calculating the electron mean free path and RRR, the relations²⁵

$$\lambda(0 \text{ K}) = \lambda_L \sqrt{1 + \frac{\pi \xi_0}{2 \ell}} \quad (13)$$

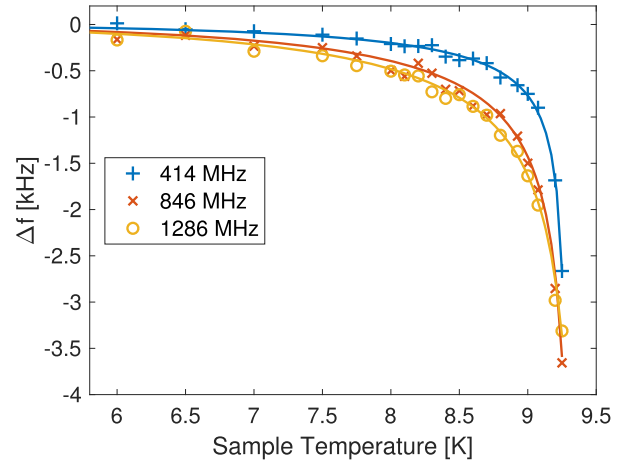


FIG. 12. Frequency-shift measurement and penetration-depth fits for three quadrupole modes recorded during one thermal cycle.

TABLE IV. Penetration depth measurement for a bulk niobium sample. The error bars give the statistical fit uncertainty.

Frequency	414 MHz	846 MHz	1286 MHz
T_c	(9.29 ± 0.01) K	(9.33 ± 0.01) K	(9.39 ± 0.09) K
$\lambda(0 \text{ K})$	(58 ± 4) nm	(67 ± 6) nm	(57 ± 7) nm
λ_L		32 nm (fixed)	Reference 25
ξ_0		39 nm (fixed)	Reference 25
ℓ	(27 ± 6) nm	(18 ± 5) nm	(27 ± 14) nm
RRR	10 ± 2	7 ± 2	10 ± 5

and³⁵

$$\text{RRR} = \frac{\ell}{2.7 \text{ nm}} \quad (14)$$

were used. The results are given in Table IV. The computed penetration depth values at all three quadrupole modes are consistent within their uncertainties. This agrees with the expectation that the superconducting penetration depth does not depend on frequency.

VI. MEASURING THE RF CRITICAL FIELD

Investigating the highest accelerating gradient achievable with a superconducting cavity, the intrinsic material limit is set by the critical magnetic (RF) field. Measuring at different temperatures gives access to both the critical field extrapolated to 0 K and the critical temperature,

$$H_{c,\text{RF}}(T) = H_{c,\text{RF}}(0 \text{ K}) \cdot \left(1 - \left(\frac{T}{T_c}\right)^2\right). \quad (15)$$

Thanks to the thermal design of the QPR sample chamber, arbitrary and highly stabilized temperatures above the liquid helium bath temperature are possible. This is especially relevant since, given by the quench limit of the QPR at about 120 mT, the sample has to be heated significantly in order to reduce its critical field.

The RF critical field is measured using single rectangular pulses of RF power. Software triggering of the RF signal generator enables

non-periodic pulses of arbitrary separation, which in turn ensures the stable sample temperature prior to each pulse. A quench suddenly decreases the quality factor of the QPR, leading to a drop in transmitted RF power. For power measurements, fast power meters (Keysight U2042XA) are used, providing a time resolution of down to 50 ns. From the trace of such a pulse, the RF quench field can directly be taken from the peak value. Figure 13 shows four exemplary pulse traces of transmitted RF power, converted to the peak RF field on the sample, for a Nb₃Sn sample. The LS336 device used to read out the temperature sensors, attached to the bottom surface of the sample, provides a maximum data rate of 10 samples/s. This is too slow to resolve the temporal evolution of the quench, but useful to distinguish between a quench of the sample or of the resonator itself.

The requirement to measure the critical field by observing a sudden decrease in transmitted power triggered by a quench puts limits on the loaded quality factor of the QPR and the measurement resolution. The unperturbed loaded quality factor of the entire system (Q_L) has to be high enough that it can be dominated by the partially normal conducting sample surface after a quench occurred. On the other hand, strong overcoupling and low values of Q_L are desired to minimize the quench time and RF heating. Assuming the initial situation of strong overcoupling ($Q_L \approx Q_{\text{input}}$) and a quenched sample quality factor of at most $Q_{s,q} = Q_{\text{input}}$, the minimum detectable quench size A_q can be estimated,

$$Q_{s,q} = \frac{\omega U}{P_{\text{sample}}} = \frac{2\omega U}{R_S A_q \hat{H}^2}, \quad (16)$$

$$A_q = \frac{2\omega U}{Q_{\text{input}} R_{S,nc} \hat{H}^2} = \frac{2\mu_0^2}{R_{S,nc} \tau_L c_2}, \quad (17)$$

with $P_{\text{sample}} \approx \frac{1}{2} R_{S,nc} \hat{H}^2 A_q$, $Q_{\text{input}} = \omega \tau_L$, and $c_2 = \mu_0^2 \hat{H}^2 / U$. $R_{S,nc}$ denotes the normal conducting surface resistance, which can vary

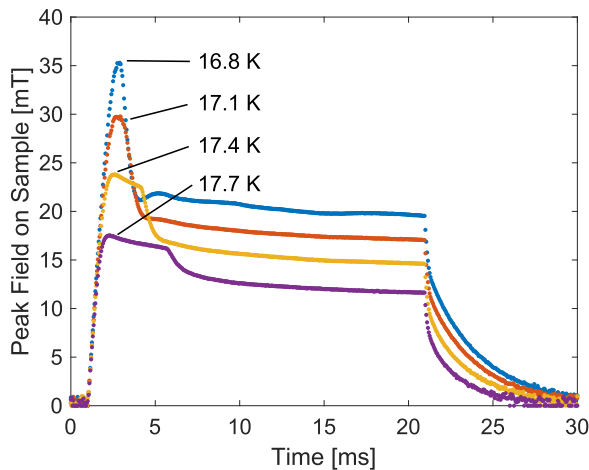


FIG. 13. Exemplary pulse traces for a Nb₃Sn sample. A constant pulse length of 20 ms was used. The RF quench field is given by the peak value. The post-quench behavior changes with temperature since it depends on thermal properties of the sample and on RF characteristics like Lorentz-force detuning and Q_L . Adapted from S. Keckert *et al.*, *Supercond. Sci. Technol.* **32**, 075004 (2019). Copyright 2019 Author(s), licensed under a Creative Commons Attribution 4.0 License.

widely, e.g., in the range of 0.6 mΩ for high-purity niobium in the anomalous limit²⁶ up to about 24 mΩ for NbTiN.³⁶ This corresponds to minimum quench sizes of $A_q = 0.7 - 29 \text{ mm}^2$ ($\tau_L = 1.8 \text{ ms}$ for the first quadrupole mode). In other words, a material-independent resolution criterion can be defined,

$$\frac{2\mu_0^2}{\tau_L c_2} = A_q \cdot R_{S,nc} = 17.5 \text{ m}\Omega \text{ mm}^2. \quad (18)$$

Investigating the pulse traces shown in Fig. 13, the actually quenched sample area can be estimated. The quench does not only decrease Q_L but also shifts the resonant frequency by several kHz, which is much larger than the cavity bandwidth of 80–100 Hz. If one assumes that the phase locked loop (PLL) loses lock for a few milliseconds (see Fig. 13), the QPR can be regarded as undriven and the decrease of stored energy is described by an exponential decay with time constant $\tau_q < \tau_L$. Since in practice $Q_{s,q} < Q_{\text{input}}$, τ_q is dominated by the quenched sample area, which can be derived using Eq. (17). If the assumption that the PLL loses lock is not valid, the decay is slowed down, leading to an underestimated quench area. This effect is visible in the pulse traces shown in Fig. 13 for $T > 17 \text{ K}$: Due to the increasing penetration depth close to T_c , the jump in resonant frequency decreases. Eventually, the PLL keeps lock and the peak in transmitted power is less distinct. In this case, fits to the post-quench behavior are meaningless to deduce the quenched sample area. A detailed analysis of the RF quench field for the Nb₃Sn sample is given in Ref. 19.

In general, a defect-free sample has to be assumed, otherwise the quench location would not be in the high-field region, leading to a significant overestimation of the actual quench field. In the high-field region, temperature differences in the vertical or horizontal direction are close to the sensor calibration accuracy and hence negligible. Note that this only applies to the situation *before* the RF pulse. More important are temperature dynamics *during* the RF rise time, which are studied in Sec. VI A.

A. Systematic error due to RF heating

The intrinsic source of systematic error for the $H_{c,RF}$ measurement technique presented above originates from RF heating during the RF rise time. Approaching T_c , the critical field becomes increasingly temperature dependent; hence, the RF rise time has to be short enough to limit RF heating to an acceptable level. Significant heating will cause the observed critical field to be underestimated systematically due to an underestimated sample temperature.

In cavity measurements, pre-quench RF heating was identified to be a major issue, even when using a MW rated klystron. Quench times of 50–200 μs led to errors due to heating of about 40%.³⁷ For the QPR, the dependence of the observed quench field on the RF rise time, and hence the amplifier forward power, was studied in a dedicated measurement. Since the term “rise time” is a characteristic quantity of the pulse shape that does necessarily tell how long the RF power is actually rising, instead the expression “quench time” (t_q) is used in the following. It measures the duration from switching on the RF power until a quench occurs. The forward power rise time can be neglected since it is less than 15 ns. Figure 14(a) shows the measured quench time as a function of forward power. A nitrogen-doped bulk niobium sample was used for this test; all points were taken

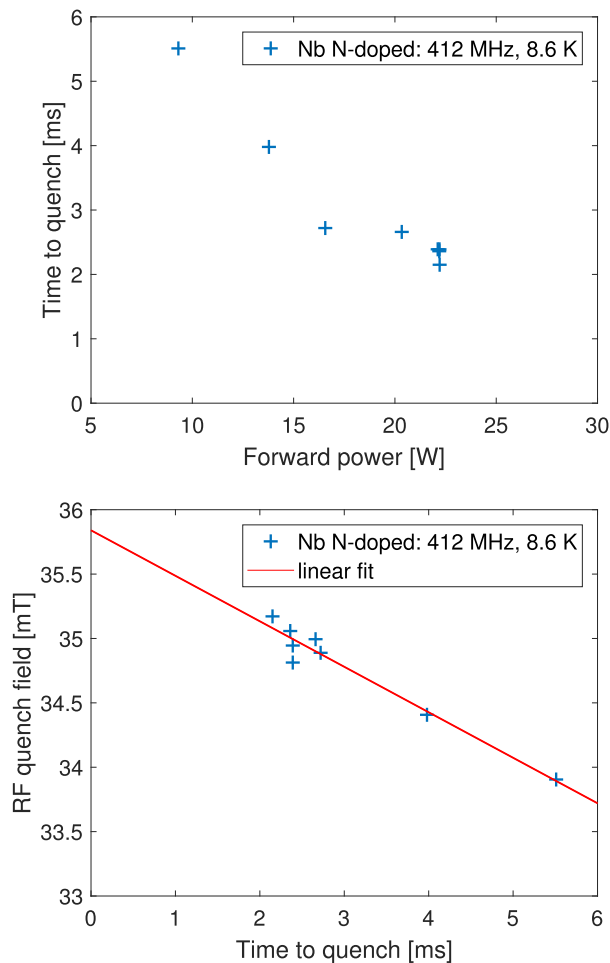


FIG. 14. Duration of the rising RF field until a quench occurs as a function of forward power (top) and corresponding RF quench field (bottom). The data were measured on a N-doped bulk niobium sample at 8.6 K and 412 MHz.

at sample temperatures of 8.6 K and 412 MHz. With increasing RF power, the quench time drops, hence reducing the possible amount of unwanted heating. More important, Fig. 14(b) shows the impact of thermal issues on the obtained quench fields. Extrapolating the linear trend for $t_q \rightarrow 0$, the systematic underestimation of $H_{c,RF}$ at $t_q = 2.5$ ms amounts to about 1 mT or 3%. This is well within the RF measurement uncertainty of about 6.5%. Furthermore, the amount of RF heating on the sample surface can be estimated: Extrapolating the value of $\mu_0 H_{c,RF}(8.6 \text{ K}, t_q = 0) = 35.8$ mT to 0 K using Eq. (15) yields $\mu_0 H_{sh} \approx 264$ mT ($T_c = 9.25$ K). Reducing the critical field at 8.6 K by 1 mT corresponds to a temperature rise of $\Delta T = 20$ mK.

Time-resolved simulations underscore the QPR's potential for critical field measurements.¹⁵ For temperature dynamics during an RF pulse, the thickness of the sample disk of 7–10 mm suppresses significantly the temperature rise when compared with values estimated for thin-walled (~ 3 mm) TESLA-type cavities. Especially when measuring at $T > 4.2$ K, single-cell cavities have to be operated in gaseous helium featuring very limited cooling. A thicker

sample, as in the case of the QPR, allows for quench times being larger by a factor of 5–10 at the same level of peak temperature rise. In turn, the required RF forward power is reduced further as compared to a TESLA-shaped single-cell cavity. Hence, one can forego using high-power klystrons for quench-field measurements in the QPR.

VII. CONCLUSION

Within the last few years, the QPR at HZB advanced from the commissioning phase to a state, where versatile, routine testing of samples to analyze a multitude of parameters is possible. The high performance in surface resistance measurements at the lowest operating RF mode was already demonstrated early on Ref. 12, while for higher harmonic modes, significant work on the RF system was needed. The measurement capabilities were continuously expanded beyond the surface resistance, enabling RF characterization of samples with respect to quench field, penetration depth, and critical temperature. From those directly measured values, quantities such as DC critical fields, mean free path, RRR, and Ginzburg–Landau parameter can be derived. Low-power measurements above T_c provide access to the bulk RRR and the normal state resistivity.

Studying the capabilities of the QPR revealed important practical and theoretical limitations that were not obvious and perhaps even counterintuitive in the design phase. Great care must thus be taken when analyzing and interpreting the data. The most important practical limitation is set by parasitic RF losses on parts of the calorimetry chamber other than on the sample surface of interest. In particular, at higher harmonic frequencies, this prevents surface resistance measurements in the low $n\Omega$ range, which, in fact, is required if fundamental limits of superconductors and possible alternative materials to niobium are investigated. Hence, the findings of this work can be used to lay out the path toward a significant evolution of a next-generation quadrupole resonator.

ACKNOWLEDGMENTS

The authors would like to thank Ernst Haebel for an inspiring and fruitful discussion about the RF design of the QPR and Sarah Aull and Tobias Junginger for discussions concerning operation and measurements. We would also like to thank Andrew Burrill for aid with the initial chemical cleaning and Jefferson Lab for providing the facilities. We would like to acknowledge the Niowave company for their support in the optimization of the mechanical design of the QPR. The research leading to these results has received funding from the European Commission under the FP7 Research Infrastructures project EuCARD-2, Grant Agreement No. 312453. This project has received funding from the European Union's Horizon 2020 Research and Innovation Programme under Grant Agreement No. 730871.

DATA AVAILABILITY

The data that support the findings of this study are available from the corresponding author upon reasonable request.

REFERENCES

- D. B. Liarte, S. Posen, M. K. Transtrum, G. Catelani, M. Liepe, and J. P. Sethna, *Supercond. Sci. Technol.* **30**, 033002 (2017).

- ²P. Goudket, T. Junginger, and B. P. Xiao, *Supercond. Sci. Technol.* **30**, 013001 (2016).
- ³C. Nantista, S. Tantawi, J. Weisend, R. Siemann, V. Dolgashev, and I. Campisi, in *Proceedings of the 21st Particle Accelerator Conference (PAC'05)* (JACoW, Knoxville, TN, 2005), pp. 4227–4229.
- ⁴B. Xiao, R. L. Geng, M. J. Kelley, F. Marhauser, H. L. Phillips, C. E. Reece, and H. Wang, in *Proceedings of the 14th International Workshop on RF Superconductivity (SRF'09)* (JACoW, Berlin, Germany, 2009), pp. 305–308.
- ⁵B. Xiao, R. Geng, M. Kelley, F. Marhauser, H. Phillips, C. Reece, and H. Wang, in *Proceedings of the 23rd Particle Accelerator Conference (PAC'09)* (JACoW, Canada, Vancouver, BC, 2009), pp. 2144–2146.
- ⁶C. Liang, L. Phillips, and R. Sundelin, *Rev. Sci. Instrum.* **64**, 1937 (1993).
- ⁷E. Brigant and E. Haebel, Numerical simulations in the design of a quadrupolar resonator Technical Note, EDMS 1178982, 1997.
- ⁸E. Brigant, E. Haebel, and E. Mahner, in *Proceedings of the 6th European Particle Accelerator Conference (EPAC'98)* (JACoW, Stockholm, Sweden, 1998), pp. 1855–1857.
- ⁹E. Chiaveri, E. Haebel, E. Mahner, and J. M. Tessier, in *Proceedings of the 6th European Particle Accelerator Conference (EPAC'98)* (JACoW, Stockholm, Sweden, 1998), pp. 1852–1854.
- ¹⁰E. Mahner, S. Calatroni, E. Chiaveri, E. Haebel, and J. M. Tessier, *Rev. Sci. Instrum.* **74**, 3390 (2003).
- ¹¹R. Kleindienst, O. Kugeler, and J. Knobloch, in *Proceedings of the 16th International Conference on RF Superconductivity (SRF'13)* (JACoW, Paris, France, 2013), pp. 614–616.
- ¹²R. Kleindienst, “Radio frequency characterization of superconductors for particle accelerators,” Ph.D. dissertation (Universität Siegen, 2017).
- ¹³B. Aune, R. Bandelmann, D. Bloess, B. Bonin, A. Bosotti, M. Champion, C. Crawford, G. Deppe, B. Dwersteg, D. A. Edwards, H. T. Edwards, M. Ferrario, M. Fouaidy, P.-D. Gall, A. Gamp, A. Gössel, J. Graber, D. Hubert, M. Hüning, M. Juillard, T. Junquera, H. Kaiser, G. Kreps, M. Kuchnir, R. Lange, M. Leenen, M. Liepe, L. Lilje, A. Matheisen, W.-D. Möller, A. Mosnier, H. Padamsee, C. Pagani, M. Pekeler, H.-B. Peters, O. Peters, D. Proch, K. Rehlich, D. Reschke, H. Safa, T. Schilcher, P. Schmüser, J. Sekutowicz, S. Simrock, W. Singer, M. Tigner, D. Trines, K. Twarowski, G. Weichert, J. Weisend, J. Wojtkiewicz, S. Wolff, and K. Zapfe, *Phys. Rev. Spec. Top.-Accel. Beams* **3**, 092001 (2000).
- ¹⁴S. Aderhold, S. Chel, E. Elsen, F. Eozenou, L. Lilje, and D. Reschke, “ILC higrade cavity process,” Technical Report No. 2010-005-1 DESY, 2010.
- ¹⁵S. Keckert, “Characterization of Nb₃Sn and multilayer thin films for SRF applications,” Ph.D. dissertation (Universität Siegen, 2019).
- ¹⁶J. Linn, “Analysis and reduction of microphonic detuning in the HZB superconducting quadrupole resonator,” B.Sc. thesis, Universität Siegen, 2017.
- ¹⁷R. Kleindienst, A. Burrill, S. Keckert, J. Knobloch, and O. Kugeler, in *Proceedings of the 17th International Conference on RF Superconductivity (SRF'15)* (JACoW, Canada, Whistler, BC, 2015), pp. 930–936.
- ¹⁸D. Tikhonov, S. Keckert, J. Knobloch, O. Kugeler, Y. Tamashevich, and A.-M. Valente-Feliciano, in *Proceedings of the 19th International Conference on RF Superconductivity (SRF'19)* (JACoW, Dresden, Germany, 2019), pp. 616–620.
- ¹⁹S. Keckert, T. Junginger, T. Buck, D. Hall, P. Kolb, O. Kugeler, R. Laxdal, M. Liepe, S. Posen, T. Prokscha, Z. Salman, A. Suter, and J. Knobloch, *Supercond. Sci. Technol.* **32**, 075004 (2019).
- ²⁰S. Keckert, D. Hall, J. Knobloch, O. Kugeler, and M. Liepe, in *Proceedings of the 18th International Conference on RF Superconductivity (SRF'17)* (JACoW, Lanzhou, China, 2017), pp. 863–866.
- ²¹S. Keckert, J. Knobloch, O. Kugeler, D. Tikhonov, and A.-M. Valente-Feliciano, in *2019 Proceedings of the 19th International Conference on RF Superconductivity (SRF'19)* (JACoW, Dresden, Germany, 2019), pp. 800–806.
- ²²S. Posen and M. Liepe, *Phys. Rev. Spec. Top.-Accel. Beams* **17**, 112001 (2014).
- ²³D. Hall, J. Kaufman, M. Liepe, R. Porter, and J. Sears, in *Proceedings of the 8th International Particle Accelerator Conference (IPAC'17)* (JACoW, Copenhagen, Denmark, 2017), pp. 40–43.
- ²⁴A. Gurevich, *Rev. Accel. Sci. Technol.* **5**, 119 (2012).
- ²⁵J. P. Turneaure, J. Halbritter, and H. A. Schwettman, *J. Supercond.* **4**, 341 (1991).
- ²⁶H. Padamsee, *RF Superconductivity: Science, Technology and Applications* (Wiley, 2009).
- ²⁷C. P. Poole, Jr., H. A. Farach, R. J. Creswick, and R. Prozorov, *Superconductivity* (Academic Press; Elsevier Ltd., 2007).
- ²⁸P. Kneisel, O. Stoltz, and J. Halbritter, *IEEE Trans. Nucl. Sci.* **18**, 158 (1971).
- ²⁹P. Kneisel, *J. Vac. Sci. Technol. A* **11**, 1575 (1993).
- ³⁰S. Keckert, J. Knobloch, and O. Kugeler, in *Proceedings of the 18th International Conference on RF Superconductivity (SRF'17)* (JACoW, Lanzhou, China, 2017), pp. 859–862.
- ³¹R. Kleindienst, S. Keckert, J. Knobloch, and O. Kugeler, in *Proceedings of the 18th International Conference on RF Superconductivity (SRF'17)* (JACoW, Lanzhou, China, 2017), pp. 867–869.
- ³²J. R. Delayen, H. Park, S. U. De Silva, G. Ciovati, and Z. Li, *Phys. Rev. Accel. Beams* **21**, 122001 (2018).
- ³³R. P. Reed and A. F. Clark, *Materials at Low Temperatures* (American Society for Metals, 1983).
- ³⁴J. Halbritter, “Fortran-program for the computation of the surface impedance of superconductors,” Technical Report No. kFK EXT 3/70-6, 1970.
- ³⁵B. Bonin, “CAS - CERN Accelerator School: Superconductivity in particle accelerators,” Report No. CERN-96-03, Hamburg, Germany, 1995.
- ³⁶A.-M. Valente-Feliciano, *Supercond. Sci. Technol.* **29**, 113002 (2016).
- ³⁷S. Posen, N. Valles, and M. Liepe, *Phys. Rev. Lett.* **115**, 047001 (2015).